Hierarchical NiCo$_2$O$_4$@nickel-sulfide nanoplate arrays for high-performance supercapacitors

Qingxin Chu [a], Wei Wang [b], Xiaofeng Wang [b], Bin Yang [a], Xiaoyang Liu [b, **],
Jiuhua Chen [a, c, *]

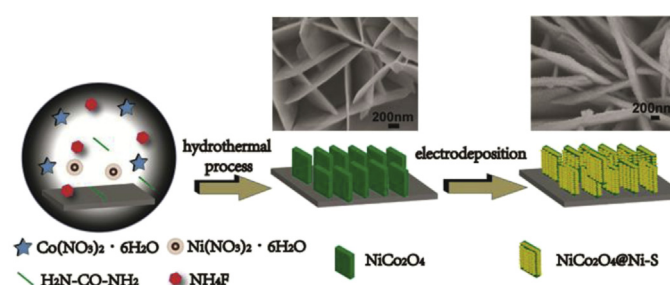[a] Center for High Pressure Science and Technology Advanced Research, Changchun 130012, China
[b] State Key Laboratory of Inorganic Synthesis and Preparative Chemistry, College of Chemistry, Jilin University, Changchun 130012, China
[c] Florida International University, Miami, FL 33199, USA

HIGHLIGHTS

- Hierarchical NiCo$_2$O$_4$@ nickel-sulfide nanoplate arrays were prepared.
- The array electrode shows good integrity and porosity.
- The array electrode exhibits an improved areal capacitance of 1.85 F cm^{-2} at 8 mA cm^{-2}.

GRAPHICAL ABSTRACT

ARTICLE INFO

ABSTRACT

Electrodeposition of nickel sulfide (Ni–S) on NiCo$_2$O$_4$ (NiCo$_2$O$_4$@Ni–S) nanoplate arrays produces a new hierarchical core–shell functional-material. Weak crystalline Ni–S nanosheets have been uniformly coated on the NiCo$_2$O$_4$ nanoplate array obtained by hydrothermal growth. When tested as an electrode for supercapacitors, the NiCo$_2$O$_4$@Ni–S nanoplate arrays have been found to exhibit a significantly improved areal capacitance of 1.85 F cm^{-2} at a current density of 8 mA cm^{-2}, good rate capability and cycling stability. In addition, the capacitance fading of the NiCo$_2$O$_4$@Ni–S arrays are attributed to the surface coarsening of the Ni–S nanosheets.

Published by Elsevier B.V.

1. Introduction

The environmental issues have pushed human being to find novel energy sources instead of fossil fuels to meet the increasing demands of energy consumptions. Currently, it is deeply urgent to develop reliable green energy storage technologies to achieve a secured and reliable energy supply. The high power performance of supercapacitors has made them important complement power sources of batteries to meet the increasing demands of energy storage and conversion [1–3]. In the two categories of super-capacitors (electrochemical double layer capacitor - EDLC and pseudocapacitor) with different charge storage mechanisms, the EDLC with traditional carbon materials has very limited specific energy. Researchers are trying to develop pseudocapacitive

materials based on faradaic reactions with the specific capacitance an order of magnitude higher than that of carbon [4,5]. To this end, metal oxides have been extensively studied as pseudocapacitor electrode materials, and it has been shown that the architecture design is very important to improve their supercapacitor performance [5,6]. In particular, 3D array electrodes have drawn much attention because of their facile preparation and excellent performance [7–9]. On the other hand, recent research results show that metal sulfides can also be used as good active materials for pseudocapacitor applications [10–12], and especially, core–shell arrays of metal oxide and sulfide have shown excellent performance [12–14]. However, the syntheses of sulfides usually involve toxic gases as reactant or product, and therefore it is very urgent to develop a green strategy to construct the core–shell oxide-sulfide array architectures.

Nickel sulfides with various compositions, such as NiS, NiS_2, Ni_3S_2, Ni_6S_5, Ni_7S_6, and Ni_3S_4 [15], are an important class of semiconductor materials with great potential multifunctional applications in high-performance supercapacitors, lithium ion batteries, and the photocatalysis production of hydrogen [15–20]. In particular, Ni_3S_2 is of interest because of its good performance as electrode materials for supercapacitors and lithium ion batteries [15,21–23]. A number of Ni_3S_2 composites, such as one-dimensional hierarchical structures of Ni_3S_2 nanosheets grown on carbon nanotube backbone [15], Ni_3S_2/graphene [24], and Ni_3S_2 nanoflakes on a 3D porous nickel foam [25], have been prepared for enhanced performance. Recently, $NiCo_2O_4$ has drawn intensive attention because of its low cost, environmental friendliness, natural abundance and importantly, a high theoretical capacitance. In addition, the $NiCo_2O_4$ array electrodes can be facilely synthesized on various substrate with excellent cycling stability, making it a good substrate to grow other pseudocapacitive materials [26]. In this paper, we demonstrate the electrodeposition of Ni–S on $NiCo_2O_4$ arrays supported by nickel foam. The $NiCo_2O_4$@Ni–S arrays were further tested as an electrode material for supercapacitors and found to exhibit a high specific capacitance of 1.85 F cm^{-2} at a current density of 8 mA cm^{-2}, good rate capability and cycling stability.

2. Experimental section

2.1. Reagents and materials

$NiCl_2 \cdot 6H_2O$, urea, $Co(NO_3)_2 \bullet 6H_2O$ and the other chemicals were purchased from Aladdin Ltd. (Shanghai, China) and used as received without further purification. The water used throughout all experiments was purified through a Millipore system.

2.2. Growing $NiCo_2O_4$ array on nickel foam

In a typical synthesis, 1 mmol of $Ni(NO_3)_2 \bullet 6H_2O$, 2 mmol of $Co(NO_3)_2 \bullet 6H_2O$, 6 mmol of NH_4F and 15 mmol of urea were dissolved in 80 mL of deionized water under magnetic stirring for 30 min in air to form a clear pink solution. 12 mL of the above solution was transferred to a 15 mL Teflon-lined stainless steel autoclave with a piece of pretreated Ni foam immersed into the reaction solution. After that, The autoclave was sealed and maintained at 120 °C for 3 h, and then cooled down to room temperature. The $NiCo_2O_4$ array coated nickel foam samples were collected and rinsed with distilled water several times, followed by annealing at 320 °C in air for 2 h. The loading mass of the $NiCo_2O_4$ nanoplate arrays is ca. 1.3 mg cm^{-2} [27].

2.3. Electrodeposition of Ni–S on $NiCo_2O_4$ array

Ni–S were synthesized by electrodeposition [25] carried out using a CHI 660D (CH Instrument) electrochemical work station in a three-electrode configuration, including a $NiCo_2O_4$ grown nickel foam as the working electrode, a Pt wire as the counter electrode and a saturated Ag/AgCl reference electrode. The electrochemical depositions of nickel sulfide nanostructure by cyclic voltammetry (CV) were performed within the potential range between −1.2 V and 0.2 V vs. Ag/AgCl at a scan rate of 5 mV s^{-1} for 10 cycles. The deposition bath used for the electrodeposition was simply composed of 50 mM $NiCl_2 \cdot 6H_2O$ and 1 M thiourea (TU). Then the as-prepared Ni–S electrodes were rinsed with deionized water and subsequently dried in vacuum at 60 °C for 12 h. The loaded weight of Ni–S film was controlled at approximately 0.8 mg cm^{-2} measured by a microbalance with an accuracy of 0.01 mg.
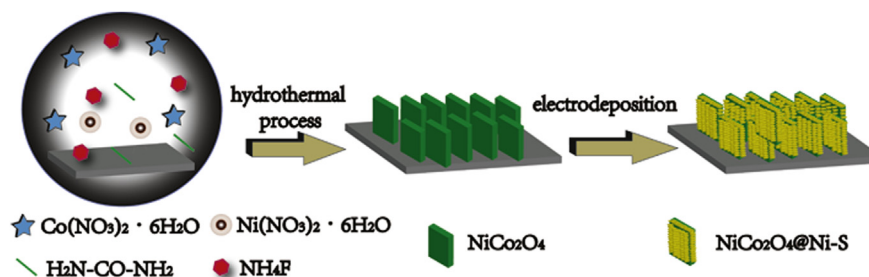
2.4. Characterizations

Powder X-ray diffraction (XRD) datum was recorded on a Rigaku D/MAX 2550 diffractometer with Cu Kα radiation (λ = 1.5418 Å). Scanning electron microscopy (SEM) images were taken with a JEOL JSM-6700F microscope operating at 10 kV. Energy-dispersive spectroscopy (EDS) was performed on an Oxford INCA energy-dispersive analyzer. X-ray photoelectron spectrophotometer (XPS) with Al-Kα radiation at 1486.6 eV (ESCALAB 250 Thermo) was used to investigate the element ratio and valence states in the synthesized samples. During each scan the C1s peak positioned at 284.6 eV was recorded as the energy reference. Transmission electron microscopy (TEM) measurements were made on a HITACHI H-8100 electron microscopy (Hitachi, Tokyo, Japan) with an accelerating voltage of 200 kV. The nitrogen sorption measurements were performed on a Micromeritics ASAP 2420 surface area analyzer by using Brunauer–Emmett–Teller (BET) method at 77 K.

2.5. Electrochemical measurements

The $NiCo_2O_4$@Ni–S arrays were directly used as the working electrode. The electrochemical tests were conducted with a CHI 660C electrochemical workstation in an aqueous NaOH electrolyte (1.0 M) with a three-electrode cell where Pt wire serves as the counter electrode and saturated calomel electrode (SCE) as the reference electrode. Electrochemical impedance spectroscopy (EIS) measurements were carried out on this apparatus with a superimposed 5 mV sinusoidal voltage in the frequency range of 100 kHz to 0.01 Hz. All the EIS measurements were acquired at the potential of 0 V vs. SCE.

3. Results and discussion

The $NiCo_2O_4$@Ni–S nanoplate arrays were synthesized by a two-step process, as illustrated in Scheme 1. Firstly, $NiCo_2O_4$ nanoplate arrays were grown on nickel foam by a hydrothermal process in an 80 mL solution containing 1 mmol of $Ni(NO_3)_2$, 2 mmol of $Co(NO_3)_2$, 6 mmol of NH_4F and 15 mmol of urea [27]. Secondly, Ni–S nanostructures were electrodeposited on the pre-grown $NiCo_2O_4$ nanoplate arrays by CV in 10 mL solution containing 50 mM $NiCl_2 \cdot 6H_2O$ and 1 M thiourea [25]. The weak-crystalline nature of the Ni–S deposit is confirmed by XRD, as shown in Fig. 1A, because the XRD patterns are nearly unchanged before and after Ni–S deposition. Electrodeposited sulfide films, for example, Co–S film with the same method of this paper, can be amorphous with no reflections in X-ray diffraction patterns [28]. In this paper, X-ray diffraction patterns present no reflections of crystalline nickel sulfides; therefore, initially, it is speculated that the Ni–S layer is

Scheme 1. Schematic illustration of the two-step synthesis of hierarchical NiCo$_2$O$_4$@Ni–S core–shell nanoplate arrays.

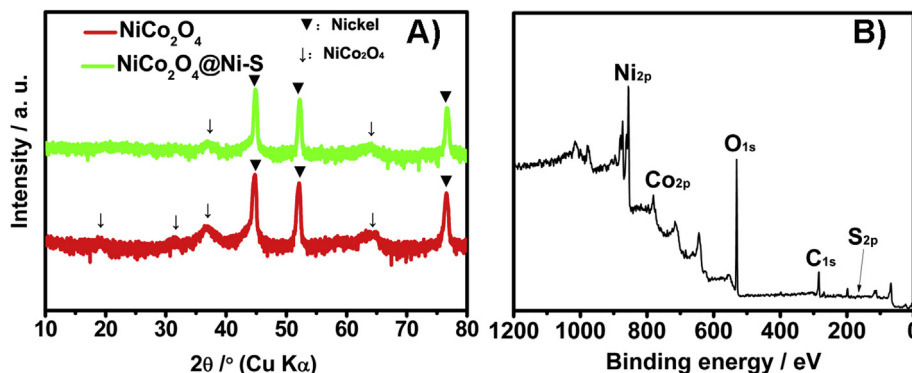**Fig. 1.** (A) Powder XRD patterns of the NiCo$_2$O$_4$ and NiCo$_2$O$_4$@Ni–S nanoplate arrays and (B) survey XPS scan of the NiCo$_2$O$_4$@Ni–S nanoplate arrays grown on nickel foam, respectively.

amorphous. However, high-resolution TEM image (Fig. S1) indicates that lattice fringes exist in some nano-regions (below 10 nm). Therefore, the Ni–S layer is weak-crystalline and the diffraction peaks may be weak and broadened, which is difficult to detect. The crystallinity of the electrodeposited Ni–S layer may be

sensitive to the substrate, leading to the different crystallinity of the Ni–S layer of this paper with the previous reported ZnO@Ni$_3$S$_2$ arrays [13]. The energy-dispersive X-ray spectra analyses show the existence of Ni, Co and O and S atoms in the final product (Fig. S2). X-ray photoelectron spectra analyses (Fig. 1B) present a Co:S ratio
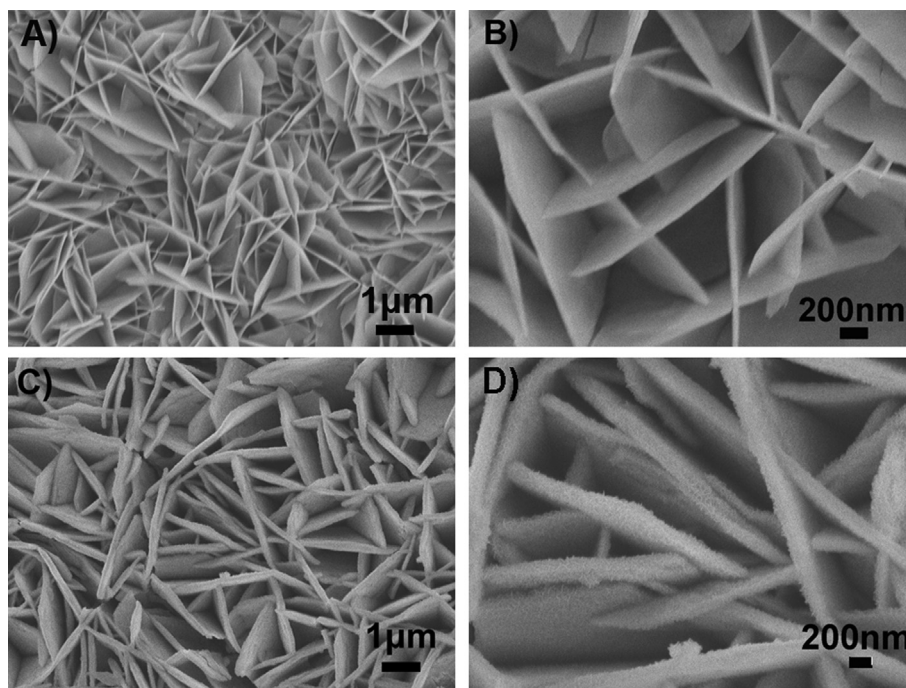

Fig. 2. SEM images of NiCo$_2$O$_4$ nanoplate (A and B) and NiCo$_2$O$_4$@Ni–S nanoplate (C and D) arrays grown on nickel foam.
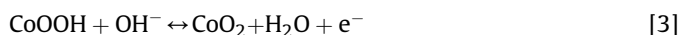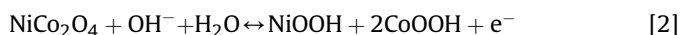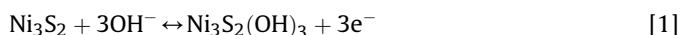
of ca 1:1, indicating the Ni:S ratio in the electrodeposited Ni–S film is ca 3:2.5, close to the composition of Ni_3S_2 in the previous studies [13,25].

Fig. 2 displays the SEM images of the $NiCo_2O_4$ and $NiCo_2O_4$@Ni–S arrays, respectively. It can be seen that the $NiCo_2O_4$ nanoplates are uniformly grown on the nickel foam skeleton, as shown in SEM image of Fig. 2A. The thicknesses of the $NiCo_2O_4$ nanoplates are around 30 nm with widths ranging from 0.5 to 1.5 μm (Fig. 2B). Fig. 2C and D shows the SEM images of the $NiCo_2O_4$ arrays after Ni–S electrodeposition. It can be seen that the $NiCo_2O_4$ arrays were uniformly covered by a thin layer nanostructures, resulting in thicker hierarchical core/shell $NiCo_2O_4$@Ni–S nanoplate arrays.

TEM images were taken to further evaluate the microstructure of the $NiCo_2O_4$ and $NiCo_2O_4$@Ni–S arrays. Fig. 3A shows the vertical $NiCo_2O_4$@Ni–S nanoplates. It can be seen that the $NiCo_2O_4$ nanoplates are covered by a thin layer nanostructure, corresponding to the SEM images of Fig. 2C and D. Fig 3B further shows an individual $NiCo_2O_4$@Ni–S nanoplate. Comparing with the individual $NiCo_2O_4$ nanoplate (Fig. 3B inset), an additional Ni–S layer can be recognized. Moreover, Fig. 3C and D further compare the $NiCo_2O_4$ and $NiCo_2O_4$@Ni–S arrays at larger magnifications, which show clearly that the $NiCo_2O_4$ nanoplate is enclosed by a thin layer of nanosheet-like morphology. The corresponding high-resolution TEM (Fig. S1) image of the shell shows lattice fringe with d-spacing of 0.2 nm, corresponding to the (202) lattice plane of Ni_3S_2 (JCPDS 44–1418). However, this reflection is not detected by XRD due to the weak-crystallinity of the Ni–S shell as discussed above. In addition, the porosity of the $NiCo_2O_4$@Ni–S nanoplates has been determined by N_2 adsorption-desorption measurements. The BET specific surface area of the $NiCo_2O_4$@Ni–S is determined to be 29.4 $m^2 g^{-1}$ with the pore size around 6 nm (Fig. S3).

The as-prepared $NiCo_2O_4$@Ni–S arrays were further evaluated as an electrode material for supercapacitors. Fig. 4A shows the CV curves of the $NiCo_2O_4$@Ni–S nanoplate arrays, $NiCo_2O_4$ arrays and bare nickel foam substrate in the voltage range of −0.2 V–0.6 V vs SCE at a scan rate of 10 mV s^{-1}. The specific capacitance is proportional to the area under the CV curve; therefore, the capacitance of the nickel foam is neglectable comparing with both array electrodes. The CV profile of $NiCo_2O_4$@Ni–S arrays clearly show pronounced pseudocapacitive characteristics comparing with $NiCo_2O_4$ array electrode. Fig. 4B further shows the CV analysis of the $NiCo_2O_4$@Ni–S nanoplate arrays at various scan rates in the potential range of −0.20−0.60 V. The couple redox peaks at around 0.38 V and 0.19 V at the scan rate of 2 mV s^{-1} can be attributed to the reversible redox reactions of Ni(II) ↔ Ni(III) and Co(III) ↔ Co(IV). It has been suggested that redox mechanism of nickel sulfide/oxides, such as Ni_3S_2 and $NiCo_2O_4$, in aqueous alkaline solution can be express as follows [25,27]:

$$Ni_3S_2 + 3OH^- \leftrightarrow Ni_3S_2(OH)_3 + 3e^- \qquad [1]$$

$$NiCo_2O_4 + OH^- + H_2O \leftrightarrow NiOOH + 2CoOOH + e^- \qquad [2]$$

$$CoOOH + OH^- \leftrightarrow CoO_2 + H_2O + e^- \qquad [3]$$

It is well-known that the ability of high-rate discharge is crucial for a supercapacitor. Fig. 4C shows the galvanostatic charge−discharge curves for the $NiCo_2O_4$@Ni–S array electrode at various current densities in the range of −0.2−0.5 V. The anodic peak at about 0.40 V from the CV curves is well manifested as a plateau in the galvanostatic charge curves. The potential plateaus observed in the charge curves correspond to the anodic process. With higher current densities, this plateau shifts to a higher voltage because of stronger polarization. The sepcific capacitance value Cs can further be estimated according to the following equation: $Cs = It/(\Delta Vm)$, where I is the current, t is the charge/discharge time, ΔV is the potential window, and m is the mass of active material. When calculate the areal capacitance, m is replaced by the area of the electrode plane, S. Fig. 4D shows the comparative galvanostatic
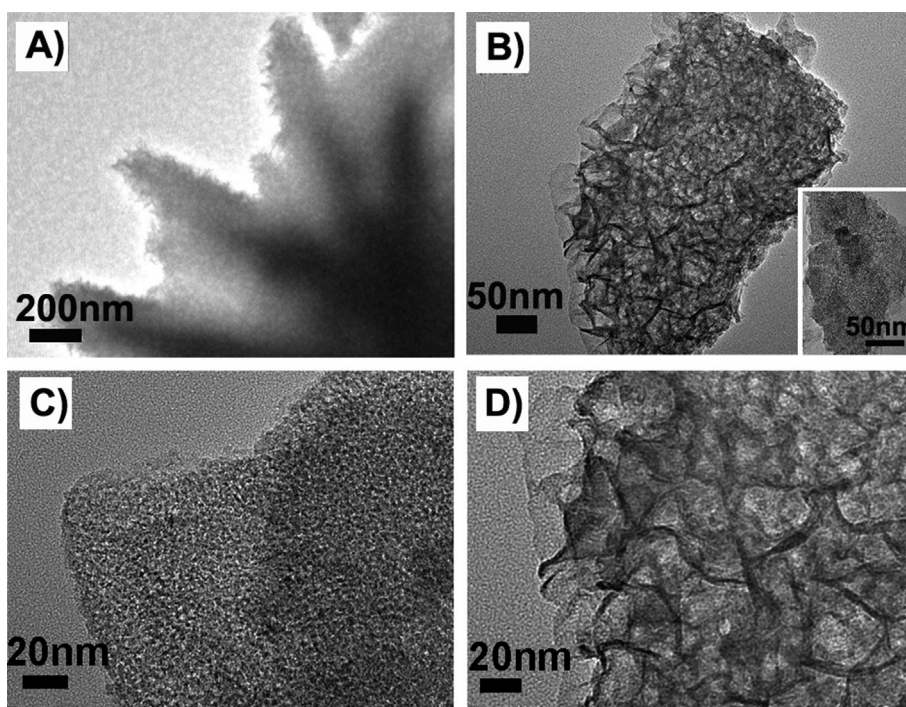

Fig. 3. TEM images of $NiCo_2O_4$@Ni–S nanoplate (A, B and D) and $NiCo_2O_4$ nanoplate (C) arrays grown on nickel foam (A presents the vertical $NiCo_2O_4$@Ni–S nanoplates and inset of B show the individual $NiCo_2O_4$ nanoplate).

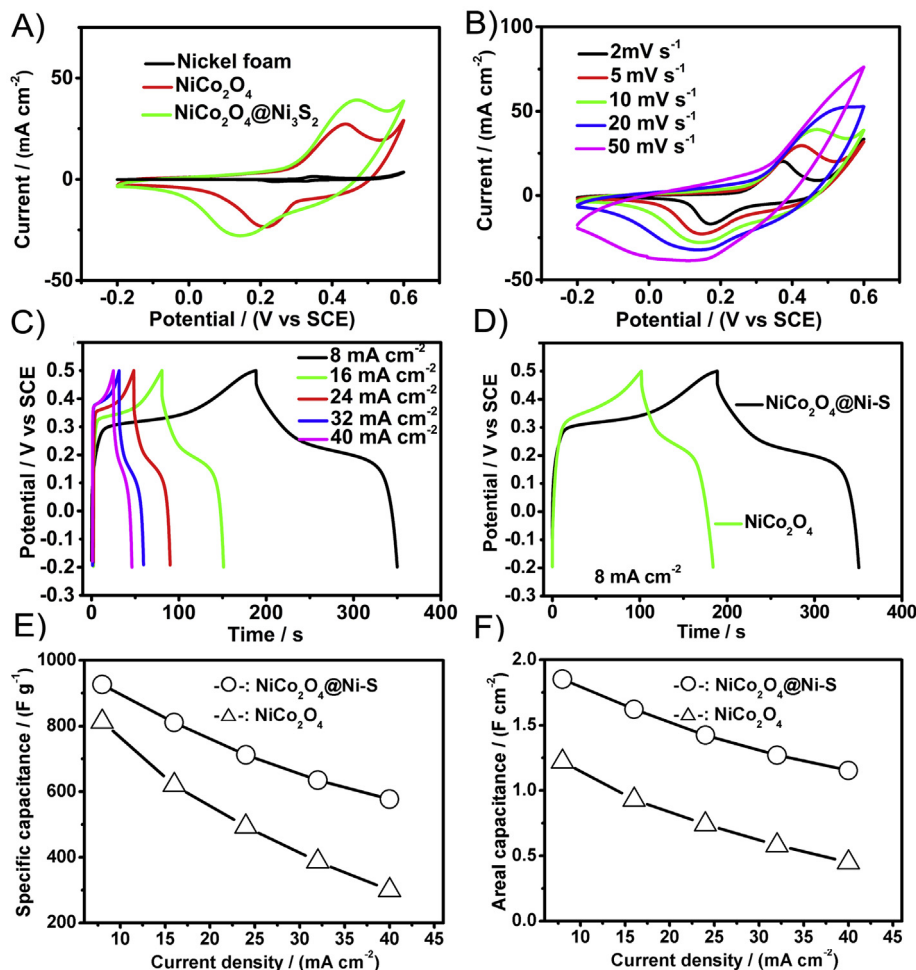**Fig. 4.** (A) CV curves of the NiCo$_2$O$_4$@Ni–S arrays, NiCo$_2$O$_4$ arrays and bare nickel foam substrate in the range of −0.20 V–0.60 V at 10 mV s^{-1}. (B) CV curves of NiCo$_2$O$_4$@Ni–S arrays in the range of −0.20 V–0.60 V at various scan rates. (C) Galvanostatic charge–discharge curves of NiCo$_2$O$_4$@Ni–S arrays at various current rates in the range of −0.20−0.50 V. (D) Galvanostatic charge–discharge curves of NiCo$_2$O$_4$@Ni–S and NiCo$_2$O$_4$ arrays at 8 mA cm^{-2} in −0.20−0.50 V. (E) Specific capacitance and (F) areal capacitance of NiCo$_2$O$_4$@ Ni–S and NiCo$_2$O$_4$ arrays at various current densities.

charge−discharge curves of NiCo$_2$O$_4$@Ni−S and NiCo$_2$O$_4$ arrays at 8 mA cm^{-2} in −0.20−0.50 V. The elongated discharging time of NiCo$_2$O$_4$@Ni−S electrode suggests its larger areal capacitance at this current density. The corresponding plots of discharge capacitance versus current density of NiCo$_2$O$_4$@Ni−S in Fig. 4C are shown in Fig. 4E and F, along with the comparative data of NiCo$_2$O$_4$ arrays. The NiCo$_2$O$_4$@Ni−S arrays can deliver a high specific capacitance of 926 F g^{-1} (1.85 F cm^{-2}) at a current density of 8 mA cm^{-2} and a specific capacitance of 577 F g^{-1} (1.15 F cm^{-2}) is still retained at a very high current density of 40 mA cm^{-2}, which are much higher than the bare NiCo$_2$O$_4$ arrays at the same current densities.

The cycling capability of the NiCo$_2$O$_4$@Ni−S array electrode was further tested by the galvanostatic charge−discharge measurements for 3000 cycles conducted at a current density of 40 mA cm^{-2} within a potential window of −0.20−0.50 V. As shown in Fig. 5A, a capacitance of 1.05 F cm^{-2} (corresponding to 71% of their initial capacitance) can be retained for the NiCo$_2$O$_4$@Ni−S arrays after 3000 cycles even at such a very high current density of 40 mA cm^{-2}. Note that the capacitance fading is mainly originated from the initial 400 cycles, which is similar to the previous report of Ni$_3$S$_2$ electrodes [13,25]. After 400 cycles the capacitance of NiCo$_2$O$_4$@Ni−S arrays was increased a little because of the electrochemical activation of NiCo$_2$O$_4$, which is ascribed to the cycling-induced improvement in the surface wetting of the electrode,

leading to more electroactive surface areas [29]. Fig. 5B further shows Nyquist plots of the NiCo$_2$O$_4$@Ni−S nanoplate arrays before and after 1000 cycles. The impedance spectrum of the NiCo$_2$O$_4$@Ni−S consists of a quasi-semicircle at higher frequency and a linear part at lower frequency. The semicircle of the Nyquist diagram corresponds to the Faradic reactions and its diameter represents the interfacial charge-transfer impedance, which was increased after 1000th cycles, corresponding to the capacitance fading in Fig. 5A. The linear part at the low frequency region in the Nyquist plots of NiCo$_2$O$_4$@Ni−S have similar angles of ~79° with the real axis (Fig. 5B), larger than typical Warburg angle of 45°, which has also been observed in the previous reports for NiCo$_2$O$_4$, and Co$_3$O$_4$ for supercapacitors [30,31]. In the present report, the obvious plateaus in the charge−discharge curves may suggest the existence of solid-state diffusion [32], as a result of the diffusive impedance of the OH$^-$ ion within the electrode [27]. In addition, a comparison of the Nyquist plots of NiCo$_2$O$_4$@Ni−S and NiCo$_2$O$_4$ arrays is shown in Fig. S4. The smaller diameter of the semicircle corresponding to the Faradic reactions of NiCo$_2$O$_4$@Ni−S nanoplate array in the Nyquist diagram indicates its smaller interfacial charge-transfer impedance than bare NiCo$_2$O$_4$ array. The above information suggests that the hierarchical core−shell structure with low electron-transfer resistance can effectively enhance electrochemical performance of the array electrodes. Fig. 5C further shows the SEM image of the
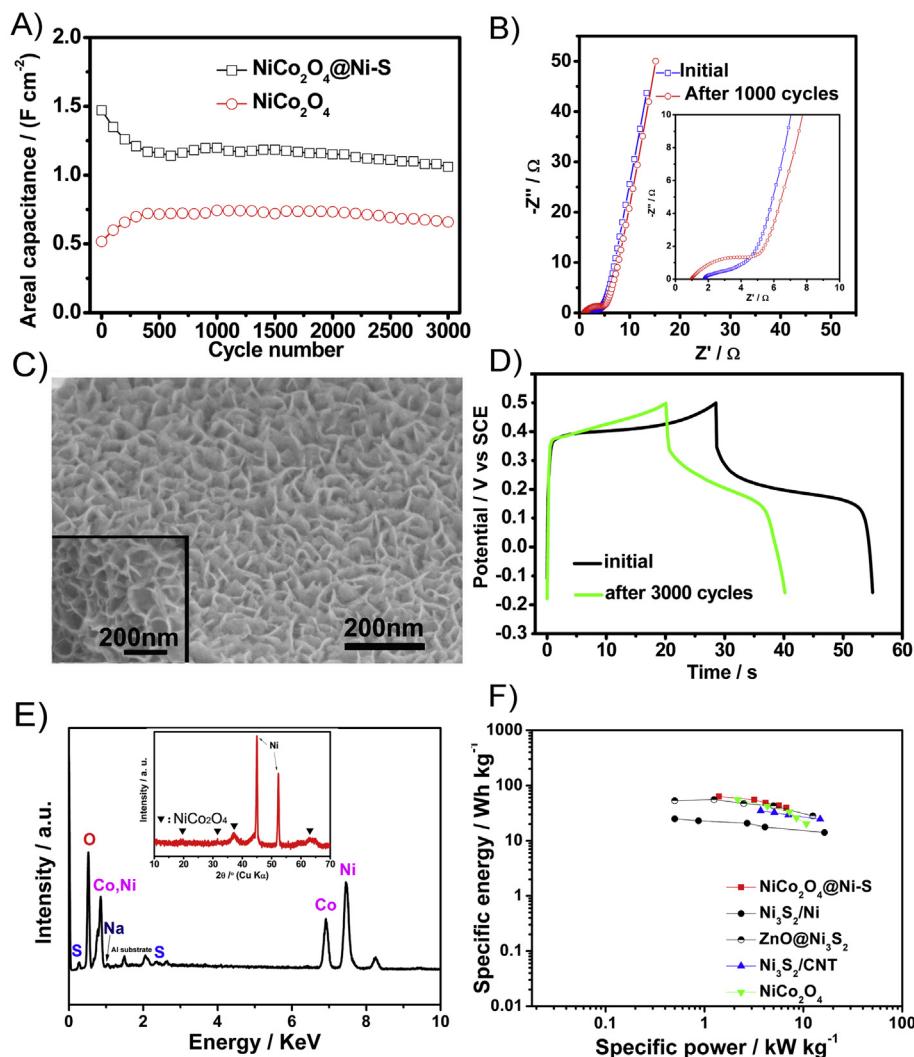
Fig. 5. (A) Cycling performance of the $NiCo_2O_4@Ni-S$ and $NiCo_2O_4$ nanoplate arrays at 40 mA cm^{-2}. (B) Nyquist plots of the $NiCo_2O_4@Ni-S$ nanoplate arrays before and after 1000 cycles. (C) SEM images of the $NiCo_2O_4@Ni-S$ nanoplate arrays before (inset) and after 3000 cycles. (D) Galvanostatic charge–discharge curves of $NiCo_2O_4@Ni-S$ arrays for the 1st and 3000th cycles. (E) EDS spectra and XRD pattern (inset) of the $NiCo_2O_4@Ni-S$ nanoplate arrays after 3000 cycles. (F) Ragone plots of the $NiCo_2O_4$ and $NiCo_2O_4@Ni-S$ nanoplate arrays, Ni_3S_2/CNT[15], $ZnO@Ni_3S_2$[13] and Ni_3S_2/Ni[25] composites.

$NiCo_2O_4@Ni-S$ nanoplate array after 3000 cycles. It can be seen that the surface of the nanoplates become coarse, as observed previously [25]. Fig. 5D shows the galvanostatic charge–discharge curves of the $NiCo_2O_4@Ni-S$ nanoplate array at 1st and 3000th cycles. After 3000 cycles, the discharge plateau becomes more inclined, which may correspond to the coarsening of the electrode surface. Elemental analysis by EDS (Fig. 5E) indicates the composition of the electrode after cycles is nearly the same as before, but there are additional trace amounts of sodium, which may be left in the electrode because of incomplete discharge, leading to capacitance fading. Usually, the specific energy of supercapacitors is between 1 and 10 Wh kg^{-1}, while the specific power can be as high as 5 kW kg^{-1} for a supercapacitor [3]. The introduction of pseudocapacitance can enhance the specific energy of the supercapacitors. The specific energy of some well-designed supercapacitor materials, for example, nickel foam/graphene/$NiCo_2O_4$ composite can reach a high value of 43.3 Wh kg^{-1} [33] and a carbon/MnO_2 system can reach 71 Wh kg^{-1} [34]. For $NiCo_2O_4@Ni-S$ nanoplate arrays, as shown in Ragone plot of Fig. 5F, the specific energy decreases from 63 to 39 Wh kg^{-1}, while the specific power increases from 1.4 to 6.7 kW kg^{-1} as the galvanostatic charge–discharge current density

increases from 8 to 40 mA/cm^{-2}. It suggests that at the same specific power, our $NiCo_2O_4@Ni-S$ nanoplate array shows the highest specific energy comparing with the previous reported $ZnO@Ni_3S_2$, Ni_3S_2/CNT and Ni_3S_2/Ni composites [13,15,25].

The excellent supercapacitive property of the hierarchical $NiCo_2O_4@Ni-S$ array electrode could be attributed to the following three reasons: (1) the $NiCo_2O_4$ arrays skeleton is stable during the processes of charging and discharging, offering effectively electron transport to Ni–S layer; (2) these electrodeposited Ni–S nanostructures are strongly anchored on the $NiCo_2O_4$ arrays to form the unique hierarchical core/shell structure with good stability and integrity; (3) the pores present within the nickel sulfides are favorable to electrolyte infiltration and the rapid diffusion of ions by providing low-resistance pathways through the electrode surface.

4. Conclusions

In conclusion, $NiCo_2O_4@Ni-S$ hierarchical core–shell nanoplate arrays have been successfully fabricated by a two-step process combining hydrothermal synthesis and electrodeposition. Such $NiCo_2O_4@Ni-S$ arrays can deliver high specific capacitances of

1.85 F cm^{-2} and 1.15 F cm^{-2} at current rates of 8 mA cm^{-2} and 40 mA cm^{-2}, respectively, and also exhibit good cycling stability. The good stability of NiCo$_2$O$_4$ arrays, the good contact between nickel sulfides and NiCo$_2$O$_4$ arrays, and the pores present within nickel sulfides are responsible for the excellent electrochemical performances of such NiCo$_2$O$_4$@Ni–S hierarchical core–shell nanoplate arrays. The present study can be extended to fabricate other oxides/sulfides core/shell arrays (for example, NiCo$_2$O$_4$@CoS$_2$, NiO@Ni$_3$S$_2$, etc.) as electrode materials for electrochemical energy storage applications.

Acknowledgments

Appendix A. Supplementary data

Supplementary data related to this article can be found at http://dx.doi.org/10.1016/j.jpowsour.2014.11.015.

References

[1] M. Winter, R.J. Brodd, Chem. Rev. 104 (2004) 4245.
[2] A. Burke, J. Power Sources 91 (2000) 37.
[3] P. Simon, Y. Gogotsi, Nat. Mater. 7 (2008) 845.
[4] M. Zhi, C. Xiang, J. Li, M. Li, N. Wu, Nanoscale 5 (2013) 72.
[5] J. Jiang, Y. Li, J. Liu, X. Huang, C. Yuan, X.W. Lou, Adv. Mater. 24 (2012) 5166.
[6] R. Liu, J. Duay, S.B. Lee, Chem. Comm. 47 (2011) 1384.
[7] J. Liu, C. Cheng, W. Zhou, H. Li, H.J. Fan, Chem. Comm. 47 (2011) 3436.
[8] X. Sun, Q. Li, Y. Lu, Y. Mao, Chem. Comm. 49 (2013) 4456.
[9] X. Xia, D. Chao, Z. Fan, C. Guan, X. Cao, H. Zhang, H.J. Fan, Nano Lett. 14 (2014) 1651.
[10] S. Peng, L. Li, C. Li, H. Tan, R. Cai, H. Yu, S. Mhaisalkar, M. Srinivasan, S. Ramakrishna, Q. Yan, Chem. Comm. 49 (2013) 10178.
[11] T. Zhu, B. Xia, L. Zhou, X. Lou, J. Mater. Chem. 22 (2012) 7851.
[12] J. Xiao, L. Wan, S. Yang, F. Xiao, S. Wang, Nano Lett. 14 (2014) 831.
[13] Z. Xing, Q. Chu, X. Ren, C. Ge, A.H. Qusti, A.M. Asiri, A.O. Al-Youbi, X. Sun, J. Power Sources 245 (2014) 463.
[14] L. Mei, T. Yang, C. Xu, M. Zhang, L. Chen, Q. Li, T. Wang, Nano Energy 3 (2014) 36.
[15] T. Zhu, H.B. Wu, Y. Wang, R. Xu, X.W. Lou, Adv. Energy Mater. 2 (2012) 1497.
[16] Z. Xing, Q. Chu, X. Ren, J. Tian, A.M. Asiri, K.A. Alamry, A.O. Al-Youbi, X. Sun, Electrochem. Comm. 32 (2013) 9.
[17] Y. Wang, Q. Zhu, L. Tao, X. Su, J. Mater. Chem. 21 (2011) 9248.
[18] S. Ni, X. Yang, T. Li, J. Mater. Chem. 22 (2012) 2395.
[19] Q. Pan, J. Xie, S. Liu, G. Cao, T. Zhu, X. Zhao, RSC Adv. 3 (2013) 3899.
[20] N. Mahmood, C. Zhang, Y. Hou, Small 9 (2013) 1321.
[21] Q. Wang, R. Gao, J. Li, Appl. Phys. Lett. 90 (2007) 143107.
[22] L. Mi, Q. Ding, W. Chen, L. Zhao, H. Hou, C. Liu, C. Shen, Z. Zheng, Dalton Trans. 42 (2013) 5724.
[23] C.-H. Lai, K.-W. Huang, J.-H. Cheng, C.-Y. Lee, W.-F. Lee, C.-T. Huang, B.-J. Hwang, L.-J. Chen, J. Mater. Chem. 19 (2009) 7277.
[24] S. Pan, J. Zhu, X. Liu, New. J. Chem. 37 (2013) 654.
[25] S.-W. Chou, J.-Y. Lin, J. Electrochem. Soc. 160 (2013) D178.
[26] G. Zhang, X.W. Lou, Adv. Mater. 25 (2013) 976.
[27] X. Liu, S. Shi, Q. Xiong, L. Li, Y. Zhang, H. Tang, C. Gu, X. Wang, J. Tu, ACS Appl. Mater. Inter. 5 (2013) 8790.
[28] Y. Sun, C. Liu, D.C. Grauer, J. Yano, J.R. Long, P. Yang, C.J. Chang, J. Am. Chem. Soc. 135 (2013) 17699.
[29] Y. Zhu, X. Ji, Z. Wu, W. Song, H. Hou, Z. Wu, X. He, Q. Chen, C.E. Banks, J. Power Sources 267 (2014) 888.
[30] M.-C. Liu, L.-B. Kong, C. Lu, X.-M. Li, Y.-C. Luo, L. Kang, X. Li, F.C. Walsh, J. Electrochem. Soc. 159 (2012) A1262.
[31] Q. Yang, Z. Lu, X. Sun, J. Liu, Sci. Rep. 3 (2013) 3537.
[32] C. Wang, A. Rakotondrainibe, A.J. Appleby, F.E. Little, J. Electrochem. Soc. 147 (2000) 4432.
[33] V.H. Nguyen, J.-J. Shim, J. Power Sources 273 (2015) 110.
[34] L. Yuan, X.-H. Lu, X. Xiao, T. Zhai, J. Dai, F. Zhang, B. Hu, X. Wang, L. Gong, J. Chen, C. Hu, Y. Tong, J. Zhou, Z.L. Wang, ACS Nano 6 (2012) 656.